processes

MDPI

Article

High Mixing Efficiency by Modulating Inlet Frequency of Viscoelastic Fluid in Simplified Pore Structure

Meng Zhang [1,†], Yunfeng Cui [2,†], Weihua Cai [1,*], Zhengwei Wu [3], Yongyao Li [1], Fengchen Li [1,4] and Wu Zhang [5,*]

1 School of Energy Science and Engineering, Harbin Institute of Technology, Harbin 150001, China; meng.zhang_china@outlook.com (M.Z.); yy-li@stu.hit.edu.cn (Y.L.); lifch@hit.edu.cn (F.L.)
2 School of Mechanical Engineering, Shanghai Jiao Tong University, Shanghai 200000, China; yunfeng.cui@sjtu.edu.cn
3 Department of Biomedical Engineering and Biotechnology, University of Massachusetts Lowell, Lowell, MA 01854, USA; zhengwei_wu@student.uml.edu
4 Sino-French Institute of Nuclear Engineering and Technology, Sun Yat-Sen University, Zhuhai 519082, China
5 School of Electrical and Electronic Engineering, Nanyang Technological University, Singapore 639798, Singapore
* Correspondence: caiwh@hit.edu.cn (W.C.); zh0002wu@outlook.com (W.Z.)
† These authors contributed equally to this work.

Received: 26 September 2018; Accepted: 16 October 2018; Published: 1 November 2018

Abstract: Fluid mixing plays an essential role in microscale flow systems. Here, we propose an active mixing approach which enhances the mixing of viscoelastic fluid flow in a simplified pore T-junction structure. Mixing is actively controlled by modulating the driving pressure with a sinusoidal signal at the two inlets of the T-junction. The mixing effect is numerically investigated for both Newtonian and viscoelastic fluid flows under different pressure modulation conditions. The result shows that a degree of mixing as high as 0.9 is achieved in viscoelastic fluid flows through the T-junction mixer when the phase difference between the modulated pressures at the two inlets is 180°. This modulation method can also be used in other fluid mixing devices.

Keywords: mixer; viscoelastic fluid; pore structure

1. Introduction

Mixing processes aim to generate a homogenous solution of multiple components in natural and engineering flows [1,2]. Such processes have been widely applied in chemical analysis [3,4], biological analysis [5,6], heat and mass transfer for microfluidic devices [7,8], fluid dynamic analysis in a porous medium [9–12], and numerous relevant small-scale research areas [13–15]. Efficient mixing is often desired for complete interaction within multicomponent systems, microreaction platforms, and mixing and transfers of small volumes at pore-scales [16,17]. Mixing can be accomplished through chaotic flow or a turbulent flow [8,18,19]; however, due to the small-scales, such flows are difficult to achieve in microfluidic systems. The realization of turbulent flow in microchannels is much more complex and challenging than in larger tubes or in open space, where the flow rate is severely limited by the driving pressure. At low flow rates, where flows are often in the laminar, low Reynolds number regime, mixing must rely on molecular diffusion between the different fluid layers, the thicknesses of which are much larger than the characteristic diffusion length. Thus, instead of relying on inertial effects, other strategies to induce mixing, like introducing the elastic effect at microscale laminar flow, may enhance the mixing effect [20].

Many microfluidic designs use fluid mechanisms to overcome the absence of turbulence [8,18,21]. These mechanisms include splitting–recombining [22], twisting [23–25], transversal flows [9], vortices [26,27], and chaotic advection [1,28–30]. These strategies can be categorized into passive and active ways [2,31,32], which depend on the application of an external energy source. They operate by the same inherent principle to generate transversal components of velocity, causing the flow to become unstable, and the thickness of fluid layers to decrease.

Mixing is also a critical process in many subsurface engineering operations, such as oil recovery [29,33]. After a secondary recovery by water flooding of a subsurface hydrocarbon reservoir, the oil and aqueous phases coexist, and additional fluid may be injected to perform enhanced oil recovery (EOR). Fluids injected during EOR include surfactant solutions [34], polymer solutions [35], and aqueous nanoparticle suspensions [36,37], and the mixing of the new aqueous fluid with the previously-injected water is an important goal of the flooding operation. In particular, polymer solutions are always applied as the final chasing fluid following other EOR fluids [38] because the high viscosity of polymer solutions can effectively suppress viscous fingering and thereby stabilize the injection front [11,39,40]. Consequently, how the chasing polymer solution mixes with the preceding EOR fluids is important in determining the overall EOR efficiency. However, in addition to being highly viscous, polymer solutions can also be viscoelastic. Viscoelasticity has been shown to significantly affect flow in porous media [41–44] or even bring about local instabilities [41,45,46]. The instability of viscoelastic fluids in porous media has been widely observed, and presents a promising opportunity for enhanced mixing [47,48], but little is understood about how to actively control these instabilities to achieve this purpose.

In this paper, we modeled a T-junction chamber as a pore element to simulate the mixing effect of unstable viscoelastic fluid flows [49–53]. The instability of the viscoelastic fluid was induced by perturbing the flow through controlled driving pressures at the inlets. This mechanism can be considered an active method for the enhancement of mixing within a microfluidic channel when the flow state is laminar and uniaxial across the pore-like channel. The driving pressure at the two inlets of the mixer was modulated by time-dependent sinusoidal signals. The degree of mixing was compared under constant pressure as well as when the pressure was modulated in one or both inlets. The effects of amplitude, frequency, and phase difference of the driving pressures were compared for viscoelastic fluid flows and Newtonian fluid flows. Finally, the results were experimentally validated using a microfluidic device.

2. Numerical Schemes

2.1. Computational Model of T-Junction Micromixer

The computational model used in this study to simulate the T-junction micromixer is shown in Figure 1. Fluid components of different concentrations flow into two inlets I_1 and I_2 from both sides of the junction and convergence begins at the junction point X. Then, the mixing fluid flows through a narrow converging channel that feeds into an expanded mixing channel where the two fluids will mix with each other. The component concentration at a cross section S in the mixing channel is monitored to determine the mixing efficiency. The length and width of the inlet channels are $L_0 = 20$ and $W_0 = 1$, respectively, while the converging channel has dimensions of $L_1 = 6$ and $W_1 = 0.5$ and the mixing channel has $L_2 = 20$ and $W_2 = 6$. The micromixer structure has a depth of $d = 1$, and the outlet is set at the end of the mixing channel.

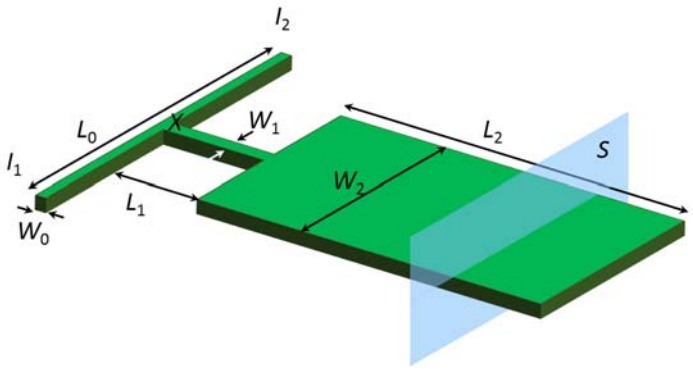

Figure 1. The computational model of T-junction micromixer.

2.2. Governing Equations

Flows in the T-junction micromixer were investigated using a solver based on the open-source software OpenFoam. The velocity, pressure, and concentration fields were numerically simulated based on the fundamental governing equations. The continuous equation and Navier–Stokes (N–S) equation were applied to solve the incompressible Newtonian fluid flow:

$$\nabla \cdot \mathbf{U} = 0 \tag{1}$$

$$\frac{\partial \rho \mathbf{U}}{\partial t} + \rho \mathbf{U} \cdot \nabla \mathbf{U} = -\nabla p + \mu \nabla^2 \mathbf{U} \tag{2}$$

where $\mathbf{U}$ represents the velocity vector of flow; p is the pressure; ρ is the density; and μ is the dynamic viscosity of the fluid.

The convection–diffusion equation was applied to solve the component concentrations in the flow:

$$\frac{\partial C}{\partial t} + \mathbf{U} \cdot \nabla C = D \nabla^2 C \tag{3}$$

where C is the component concentration of the fluid and D is the diffusion coefficient of fluid.

For the incompressible viscoelastic fluid flow, the N–S equation is modified as:

$$\frac{\partial \rho \mathbf{U}}{\partial t} + \rho \mathbf{U} \cdot \nabla \mathbf{U} = -\nabla p + \mu \nabla^2 \mathbf{U} + \nabla \cdot \boldsymbol{\tau}_p \tag{4}$$

where $\boldsymbol{\tau}_p$ is the elastic stress, which can be derived from the constitutive equation of viscoelastic fluid. The constitutive equation describes the relation between molecule deformation and elastic stress in the fluid:

$$\boldsymbol{\tau}_p = k_B T (f(r)\mathbf{C} - \mathbf{I}) \tag{5}$$

where k_B is the Boltzmann constant; T is the absolute temperature of the fluid; $f(r)$ is the Peterlin function; $\mathbf{C}$ is the conformation tensor of polymer molecules; and $\mathbf{I}$ is the Kronecker symbol for the unit tensor. The constitutive equation is further derived from Equation (5) as:

$$\boldsymbol{\tau}_p = \eta_p (f(r)\mathbf{C} - \mathbf{I})/\lambda \tag{6}$$

where η_p is the solute viscosity and λ is the relaxation time of the solution. The transport equation of the conformation tensor is then expressed as:

$$\frac{\partial \mathbf{C}}{\partial t} + \mathbf{U} \cdot \nabla \mathbf{C} = \mathbf{C} \cdot \nabla \mathbf{U} + (\nabla \mathbf{U})^T \cdot \mathbf{C} - [\mathbf{I} + \alpha(\mathbf{C} - \mathbf{I})] \cdot [f(r)\mathbf{C} - \mathbf{I}]/\lambda \tag{7}$$

where α is a parameter that relates to the anisotropy of drag encountered by flowing polymer segments [54]. Different $f(r)$ and α are selected in different constitutive models. Here, we assumed

that the viscoelastic fluid is linearly extended during the flow, so that $f(r) = 1$ and $\alpha = 0$. This satisfies the flow situation of a Boger fluid in the Oldroyd-B constitutive model. Therefore, Equations (6) and (7) are simplified as:

$$\boldsymbol{\tau}_p = \eta_p(\mathbf{C} - \mathbf{I})/\lambda \tag{8}$$

$$\frac{\partial \mathbf{C}}{\partial t} + \mathbf{U}\cdot\nabla\mathbf{C} = \mathbf{C}\cdot\nabla\mathbf{U} + (\nabla\mathbf{U})^T\cdot\mathbf{C} - \mathbf{I}\cdot(\mathbf{C} - \mathbf{I})/\lambda \tag{9}$$

Moreover, in order to gain more universal computational results, the dimensionless governing equations were used based on the following:

$$\nabla^* = H\cdot\nabla,\ \mathbf{U}^* = \frac{\mathbf{U}}{U_i},\ t^* = \frac{tU_i}{H},\ p^* = \frac{p}{\rho {U_i}^2},\ C^* = \frac{C}{C_{\max}} \tag{10}$$

where H is the hydraulic diameter of the channel; U_i is the center velocity of the fluid at the inlet channel; ρ is the fluid density; and C is the component concentration in the fluid. We defined the dimensionless Reynolds number Re and Schmidt number Sc as:

$$Re = \frac{\rho U_i H}{\mu},\ Sc = \frac{\nu}{D} \tag{11}$$

where ν is the kinematic viscosity of the fluid. The dimensionless governing continuous equation and the N–S equation can then be expressed as:

$$\nabla^*\cdot\mathbf{U}^* = 0 \tag{12}$$

$$\frac{\partial \mathbf{U}^*}{\partial t^*} + \mathbf{U}^*\cdot\nabla^*\mathbf{U}^* = -\nabla^* p^* + \frac{1}{Re}\nabla^{2*}\mathbf{U}^*, \tag{13}$$

and the convection–diffusion equation is expressed as:

$$\frac{\partial C^*}{\partial t^*} + \mathbf{U}^*\cdot\nabla^* C^* = \frac{1}{Re\cdot Sc}\nabla^{2*} C^* \tag{14}$$

Meanwhile, for a viscoelastic fluid, we defined the dimensionless parameter Weissenberg number Wi and the viscosity ratio β as:

$$Wi = \frac{\lambda U_i}{D}, \beta = \frac{\eta_s}{\eta_s + \eta_p} \tag{15}$$

where λ is the relaxation time of the viscoelastic fluid; η_p is the solute kinetic viscosity; η_s is the solvent kinetic viscosity. Thus, the dimensionless N–S equation for viscoelastic fluid flow and the conformation tensor transport equation are modified as:

$$\frac{\partial \mathbf{U}^*}{\partial t^*} + \mathbf{U}^*\cdot\nabla^*\mathbf{U}^* = -\nabla^* p^* + \frac{\beta}{Re}\nabla^{2*}\mathbf{U}^* + \frac{1-\beta}{ReWi}\nabla^*\mathbf{C} \tag{16}$$

$$\frac{\partial \mathbf{C}}{\partial t^*} + \mathbf{U}^*\cdot\nabla^*\mathbf{C} = \mathbf{C}\cdot\nabla^*\mathbf{U}^* + (\nabla^*\mathbf{U}^*)^T\cdot\mathbf{C} - \frac{\mathbf{I}\cdot(\mathbf{C} - \mathbf{I})}{Wi} \tag{17}$$

For both Newtonian fluid and viscoelastic fluid cases, the dimensionless density, dimensionless viscosity, and Re were all set at 1.0, while Sc was set at 10^{-8}. In addition, in the viscoelastic fluid case, the dimensionless relaxation time λ was set at 5.0, the dimensionless solution viscosity was set at 0.4, and dimensionless solvent viscosity was set at 0.6.

2.3. Numerical Methods

In this work, the fluid in the micromixer initially had a component concentration of 0. The dimensionless component concentration C_1 was 0 for the fluid entering through inlet I_1, while $C_2 = 1$ for the fluid entering through inlet I_2. The driving pressure is P_1 at inlet I_1 and P_2 at inlet I_2.

The no-slip condition was imposed on all channel surfaces, and a fully developed flow condition was used at the mixer outlet.

The first-order Euler implicit scheme was used for time marching in the unsteady transport equations of Equations (14), (16), and (17), with a small dimensionless time step $\delta t = 10^{-3}$. The convection terms in Equations (14) and (16) were discretized by the QUICK scheme, while the bounded MINMOD scheme was used to discretize the convection terms in Equation (17). Pressure–velocity coupling was handled by the PISO algorithm.

2.4. The Definition of Mixing Efficiency

Given component concentrations $C_1 = 0$ and $C_2 = 1$, a full mixing of the two fluids will result in a concentration of 0.5 when two averaged flow rates are the same. The degree of mixing is calculated by taking the standard deviation of concentration at all meshed points in cross-section S, defined as:

$$A = \sqrt{\sum_{i=1}^{N} \frac{(x_i - E)^2}{N}} \tag{18}$$

where N is the number of meshed points in the cross-section; x_i is the concentration at point i; and E is the full mixing concentration, which is 0.5. Equation (18) is valid if the fluid density at each mesh point is the same. However, the flow rate is higher at the center of the channel and lower at the channel sides due to the no-slip boundary condition and fluid viscosity. Therefore, the deviation needs to be adjusted as:

$$B = \sqrt{\sum_{i=1}^{N} \frac{(x_i - E)^2}{N} \frac{V_i}{V_{mean}}} \tag{19}$$

where V_i is the velocity at the mesh point i and V_{mean} is the average velocity in cross-section S. B ranges from 0 to 0.5, where $B = 0$ means full mixing while $B = 0.5$ indicates no mixing. We then define the degree of mixing as:

$$M = 1 - \frac{\sqrt{\sum_{i=1}^{N} \frac{(x_i - E)^2}{N} \frac{V_i}{V_{mean}}}}{\mu} \tag{20}$$

Therefore, $M = 1$ indicates full mixing, while $M = 0$ when no mixing occurs. We will use this index to present the mixing efficiency in the following sections.

3. Results and Discussion

3.1. Mixing in Condition of Constant Pressure

We first investigated fluid mixing in the T-junction micromixer when both inlets I_1 and I_2 are under the same constant pressure $P_0 = 3500$. Figure 2a,b compare the component concentration distribution in the Newtonian fluid and viscoelastic fluid cases after the fluid has flowed in the micromixer for a long time ($t = 120$). The color map indicates the normalized component concentration (red represents C = 1 and blue represents C = 0). It can be seen that the two injected fluids are well separated in the converging channel. In the mixing channel, green appears at the center area along the flow direction. The concentration gradually changed between 0 and 1 and reached 0.5 in the center, indicating a high mixing here. Compared to the Newtonian fluid case, the mixing area is larger in the viscoelastic fluid. Since the simulation conditions for two fluids were identical except that the viscoelastic fluid had a nonzero elasticity, the improvement in mixing must originate from elastic stress in the viscoelastic fluid.

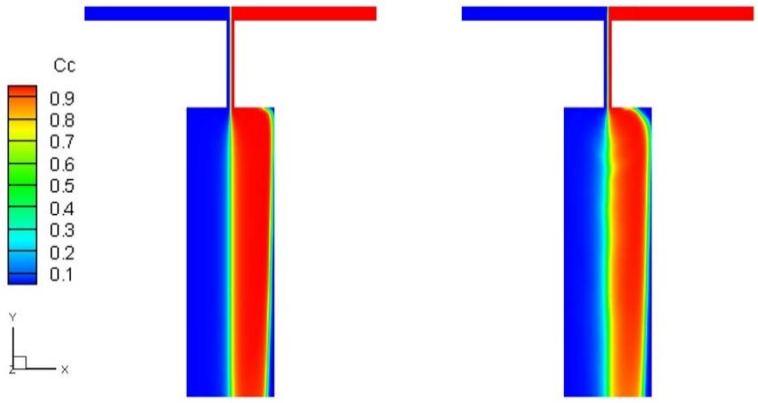

Figure 2. Concentration distribution in the Newtonian fluid case (**a**) and viscoelastic fluid case (**b**) under constant driving pressure at both inlets.

The elastic stress effect was further confirmed by investigating the flow streamlines and fluid angular velocity, as shown in Figure 3. In the Newtonian fluid case, the streamlines bend 90° downward at the convergence point and there is no angular velocity in the flow. By contrast, the streamlines in viscoelastic fluid in the same region first bend up slightly before bending down. A nonzero angular velocity is observed in the narrow channel, indicating convection of two viscoelastic fluids and more significant mixing. The degree of mixing M was analyzed at the cross-section S, which was set at a distance of L_s = 12 below the channel expansion point. For both cases, M increases until it becomes stable starting from t = 80, but their magnitudes differ: M plateaus at 0.15 for the Newtonian fluid case and 0.25 for the viscoelastic fluid case, as shown in Figure 4. This quantitatively shows that mixing was improved in viscoelastic fluid case.

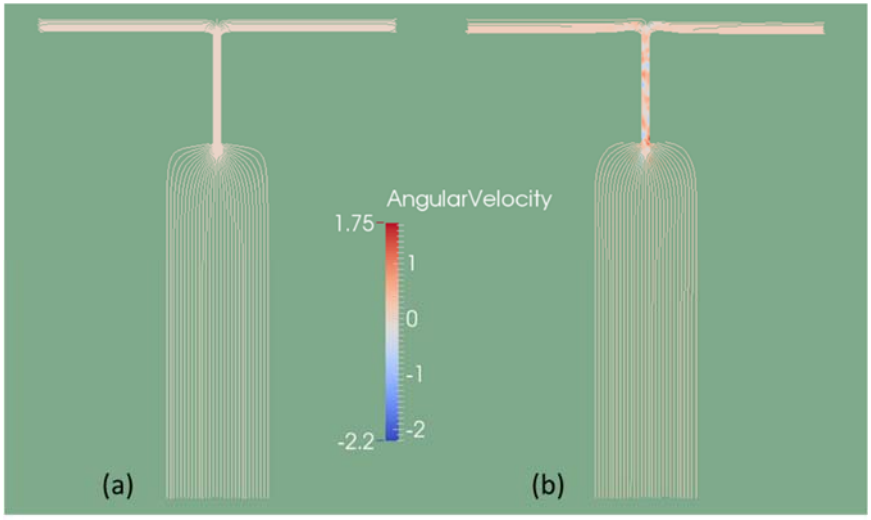

Figure 3. Streamlines and angular velocity in the Newtonian fluid case (**a**) and viscoelastic fluid case (**b**) under constant driving pressure at both inlets.

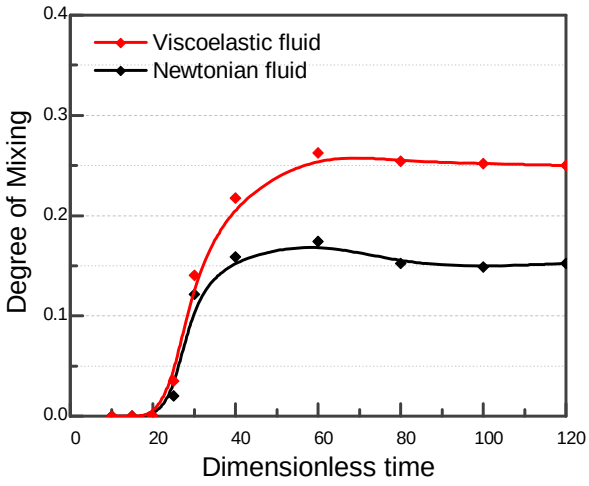

Figure 4. Degree of mixing in the Newtonian fluid case (**black line**) and viscoelastic fluid case (**red line**) under constant driving pressure at both inlets.

3.2. Mixing in Single-Side Pressure Oscillation

We modulated the driving pressure P_1 at inlet I_1 with a sinusoidal factor while keeping the pressure P_2 at inlet I_2 constant:

$$P_1(t) = P_0[1 + A\sin(2\pi f t)] \tag{21a}$$

$$P_2 = P_0 \tag{21b}$$

where A and f are the amplitude and frequency of the modulating signal, respectively. A, f, and P are all dimensionless. A was set at 0.8 to ensure a large pressure modulation while keeping the absolute pressure positive during the driving process. f was set at 1. P_0 was the same as that in the constant pressure case, 3500. The change in the degree of mixing in cross-section S within one period was studied when pressures in Equation (21) were applied to the viscoelastic fluid case. Under the above driving pressure, the concentration distributions at t = 120 in the Newtonian fluid and viscoelastic fluid cases are shown in Figure 5, respectively. The transition region between the blue (low concentration) and red (high concentration) fluids expanded significantly when the pressure was modulated compared to when the pressure was constant, indicating that pressure modulation greatly improves mixing efficiency. Meanwhile, the concentrations in the converging channel were no longer uniformly distributed along the channel due to the pressure changes over time. At times $P_1 < P_2$, higher concentration fluid from inlet I_2 will enter the converging channel. The converse happens when $P_1 > P_2$. In other words, the two fluids will alternatively enter the mixing channel in larger amounts. Due to the large width of the subsequent expanded channel, the small amounts of fluids introduced during one pressure cycle will start to expand and convect with each other. In this way, better mixing can be realized. In addition, we can also see that the larger discontinuous portion of fluid alternated more in the converging channel for the viscoelastic fluid case compared to the Newtonian fluid case, which indicates a higher mixing efficiency in the viscoelastic fluid. This was confirmed by investigating the degree of mixing at the cross-section S for both fluids. Figure 6 compares the mixing of a viscoelastic fluid with a different relaxation time and a Newtonian fluid. Mixing increased with the relaxation time and became stable at t = 80 for all fluids. The Newtonian fluid had the lowest degree of mixing of 0.62. Mixing gradually increased from 0.63 to 0.70 as the relaxation time λ increased from 1 to 10. This is because a higher relaxation time indicates a larger elastic stress, which leads to more convection in the fluid. Compared to the condition of constant pressure, the degree of mixing increased from 0.15 to 0.61 for the Newtonian fluid case under modulated pressure and from 0.25 to 0.68 for a viscoelastic fluid with λ of 5.

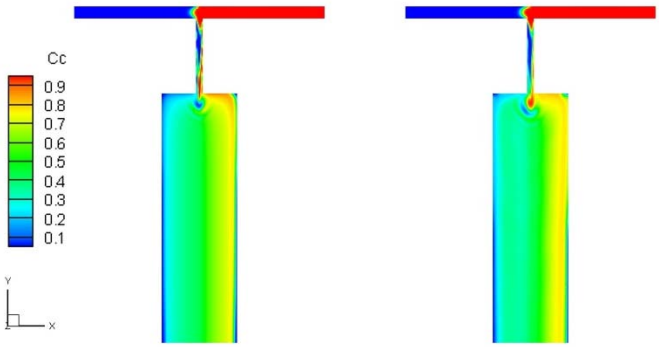

(**a**) (**b**)

Figure 5. Concentration distribution in the Newtonian fluid case (**a**) and viscoelastic fluid case (**b**) under modulated pressure at the inlet I_1 and constant pressure at the inlet I_2.

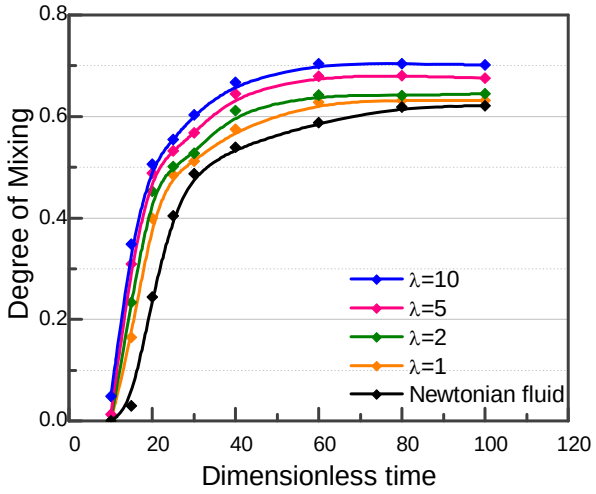

Figure 6. Degree of mixing in the Newtonian fluid case and viscoelastic fluid case with different relaxation time under modulating driving pressure at the inlet I_1 and constant pressure at the inlet I_2.

The flow streamlines and flow angular velocity were also investigated within one period, shown in Figure 7a,b for the Newtonian fluid case and Figure 7c,d for the viscoelastic fluid case. For both fluids, the stream flowed mainly from inlet I_1 at t = 119.2 (Figure 7a,c) and mainly from inlet I_2 at t = 119.7 (Figure 7b,d). The streamlines were smooth, and no angular velocity was observed in the Newtonian fluid case. However, the viscoelastic fluid formed flow vortexes alternating between the right and left sides of convergence points at times t = 119.2 and t = 119.7, respectively. The fluctuation in flow vortexes indicates enhanced convection between two fluids, which in turn leads to better mixing.

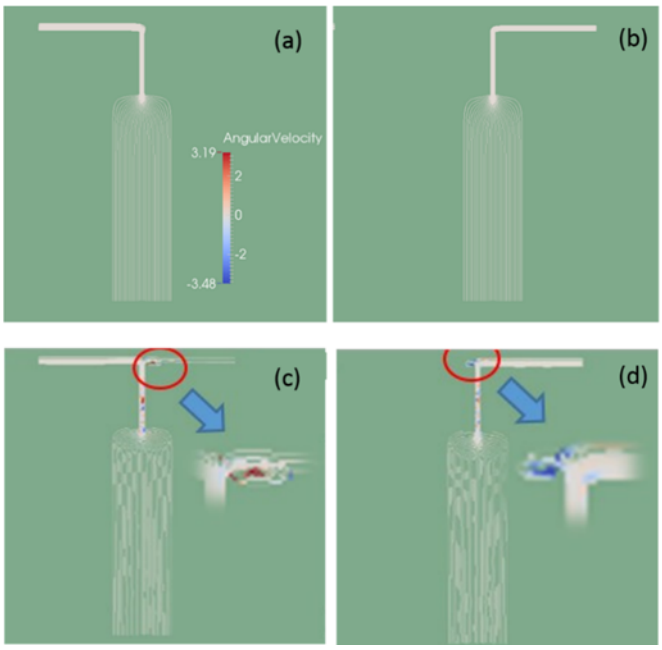

Figure 7. Streamlines and angular velocity in the Newtonian fluid case (**a**,**c**) and viscoelastic fluid case (**b**,**d**) under modulated pressure at the inlet I_1 and constant pressure at the inlet I_2.

3.3. Mixing in Double-Sided Pressure Oscillation

Since a single inlet modulation improves mixing, we next investigated the effect of modulating the driving pressure at both inlets. Here, we modulated both driving pressures P_1 and P_2 with sinusoidal signals of the same amplitude A and frequency f, but with independent phase delays φ_1 and φ_2:

$$P_1(\mathrm{t}) = P_0[1 + A\sin(2\pi f\mathrm{t} + \varphi_1)] \tag{22a}$$

$$P_2(\mathrm{t}) = P_0[1 + A\sin(2\pi f\mathrm{t} + \varphi_2)] \tag{22b}$$

and we examined the dependence of mixing on A, f, and $\Delta\varphi = \varphi_1 - \varphi_2$, the phase difference between the two pressures.

Setting $A = 3500$ and $f = 1$, the concentration distribution of viscoelastic fluid when $\Delta\varphi$ varies from 0 to π was investigated at $t = 120$, shown in Figure 8. The high and low concentration fluids are symmetrically distributed on both sides of the T-junction when $\Delta\varphi = 0$ (Figure 8a) because the driving pressure at both inlets is always the same. Only very small amounts of the two fluids mix with each other along the center of the channel. However, the distribution symmetry is broken as $\Delta\varphi$ starts to increase. A small fluctuation of the fluids in the converging channel was observed when $\Delta\varphi = \pi/6$, and it was magnified at the expansion point when the fluids entered the expanded channel, as shown in Figure 8b. As a consequence, the size of the mixing region starts to increase. As $\Delta\varphi$ is increased to $\pi/3$, the two fluids start to alternate along the converged channel (Figure 8c) and the blue and red flows start to become discontinuous at the expansion point. Furthermore, the green region increases, while narrow streams of the low and high concentration fluids remain observable near the left and right sidewalls, respectively. As $\Delta\varphi$ is further increased to $\pi/2$ (Figure 8d), the green region occupies most of the expansion channel, and isolated spots of unmixed fluid appear at the expansion point, as shown in the insert of Figure 8d. This means that the instantaneous pressure difference between the two inlets was large enough to allow the fluids to enter the converged channel separately. For $\Delta\varphi$ between $2\pi/3$ to π (Figure 8e–g), the green region occupies almost all of the expansion channel, indicating good mixing. The degree of mixing for different $\Delta\varphi$ is plotted in Figure 9. When $\Delta\varphi = 0$, the mixing degree stabilizes at 0.2 after $t = 20$. The stabilization time t increases to 40, 60 and 80 for $\Delta\varphi$ of $\pi/6$, $\pi/3$, and $\pi/2$, respectively, and the corresponding maximum degrees of mixing increase to 0.45,

0.63 and 0.73, respectively. The degree of mixing reaches a system-wide maximum value of 0.82 when $\Delta\varphi = \pi$. A phase difference of π maximizes the difference in the amount of fluid entering from each inlet at any instant in time. The fluid volumes alternate during each period, and this alternating fluid pattern expands in the wide mixing channel. As a result, the diffusion area is increased. By contrast, when $\Delta\varphi = 0$, the fluids from the inlets flow side by side along the channel direction and the diffusion area is only along the length of the center line.

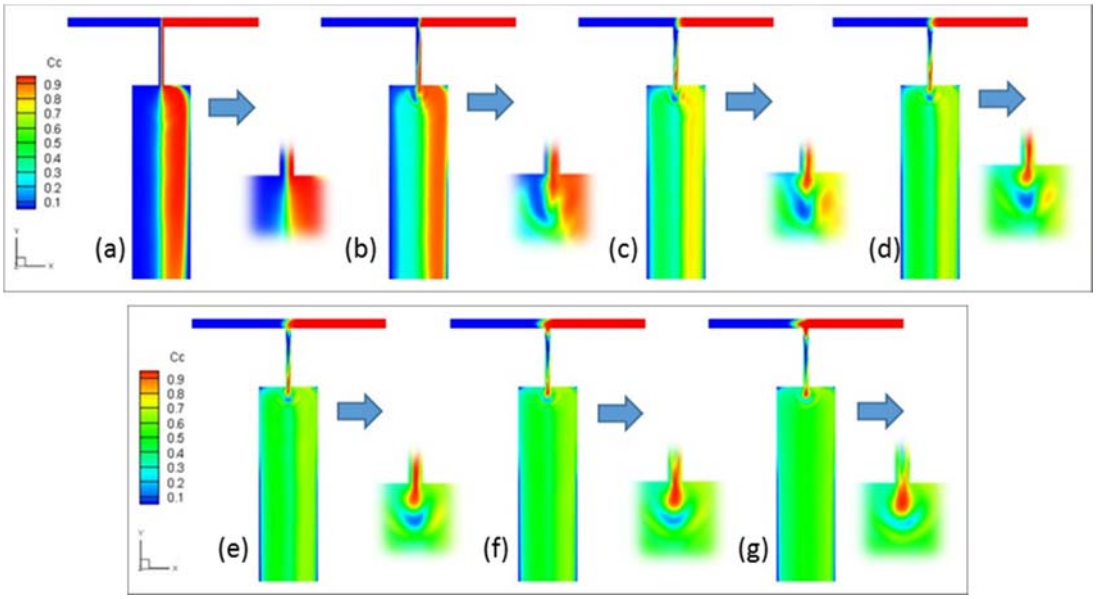

Figure 8. Concentration distribution in viscoelastic fluid case under modulated pressure at both inlets with phase difference (**a**) 0, (**b**) $\pi/6$, (**c**) $\pi/3$, (**d**) $\pi/2$, (**e**) $2\pi/3$, (**f**) $5\pi/6$, and (**g**) π.

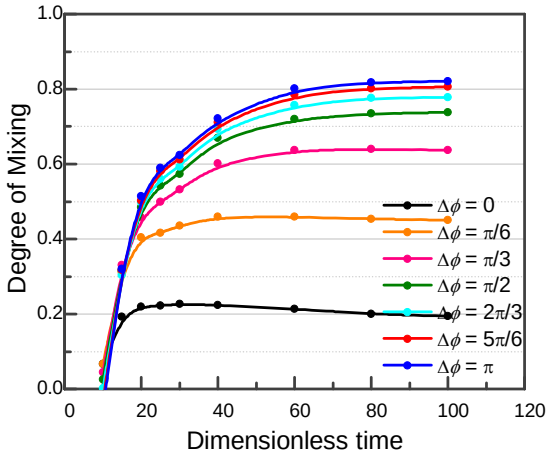

Figure 9. Degree of mixing in viscoelastic fluid case under modulated pressure at both inlets with phase difference from 0 to π.

At a higher frequencies, less fluid will enter the converged channel during each period. As shown in Figure 10a,b, the component mixing maps are compared for the viscoelastic fluid case when $f = 1$ and $f = 1.5$, respectively, with fixed parameters $A = 3500$ and $\Delta\varphi = \pi$. The green region shrinks significantly when f increases from 1 to 1.5. In addition, larger regions of unmixed fluid occupy the left and right sides of the expanded channel. This indicates that a higher modulating frequency undermines the mixing effect. This can be better understood by looking at the concentration distributions in the inlets and in the converging channel. At time $t = 120$, the pressure at inlet I_2 is higher than that at inlet I_1, and more of the red fluid will be injected. At a lower modulating frequency, the difference in the amount of

fluid flowing into the converging channel from each side is larger in each cycle; this can be observed in the converging channel and results in a higher mixing efficiency overall. The final degrees of mixing, which increase from 0.61 to 0.90 as the pressure oscillation frequency decreases from $f = 2$ to $f = 0.5$, are shown in Figure 11.

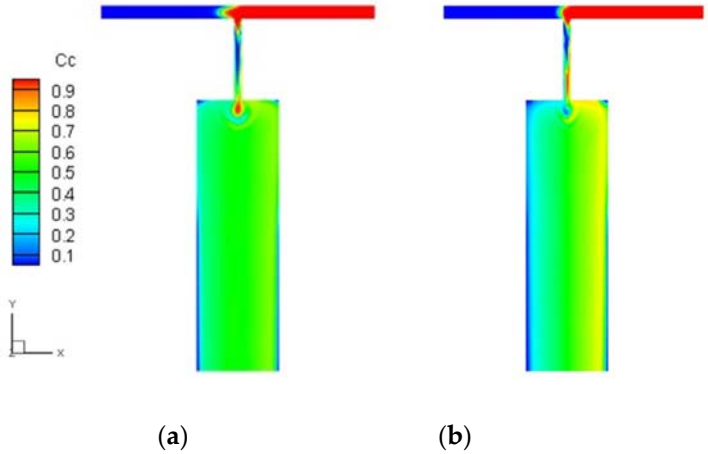

Figure 10. Concentration distribution in viscoelastic fluid case under modulated pressure at both inlets with modulating frequency of $f = 1$ (**a**) and $f = 1.5$ (**b**).

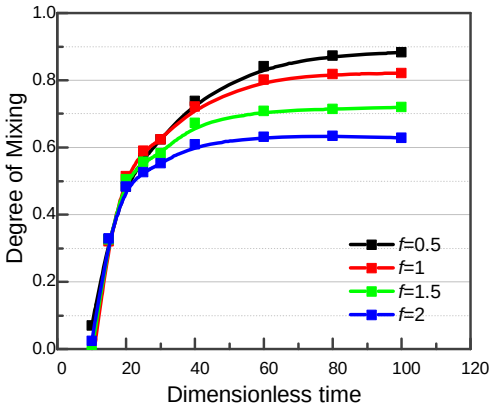

Figure 11. Degree of mixing in viscoelastic fluid case under modulated pressure at both inlets with different modulating frequencies.

In addition, we can also increase the degree of mixing by increasing the alternating volume within one cycle using a higher pressure level at the inlets. To do this, P_0 in Equation (22) is varied between 3500 to 6000 while setting $f = 1$ and $\Delta\varphi = \pi$. By increasing P_0, the final degree of mixing in the viscoelastic fluid case also increases from 0.82 to 0.91, as shown in Figure 12.

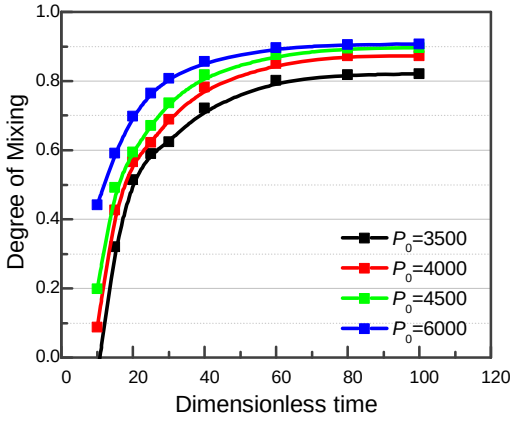

Figure 12. Degree of mixing in viscoelastic fluid case under modulated pressure at both inlets with different amplitudes.

4. Experimental Results

To validate the results of the simulations, the mixing efficiency was experimentally studied here in a PDMS-glass bonded microfluidic chip, as shown in Figure 13a. A mold for the PDMS structure was fabricated from SU8 photoresist on a silicon wafer using a standard photolithography process. The PDMS is a mixture of base and crosslinker with a ratio of 10:1. It was poured on the SU8 mold and cured at 65 °C for 4 h. To complete the chip, the cured PDMS was bonded to a glass slide after oxygen plasma treatment. The size of the microchannel was scaled to 100 μm based on the model in Figure 1. The length and width of the inlet channel were L_0 = 2 mm and W_0 = 100 μm, respectively. The converging channel was L_1 = 600 μm in length and W_1 = 50 μm in width. The mixing channel was L_2 = 2 mm in length and W_2 = 600 μm in width. The entire micromixer structure had a depth of d = 100 μm, and the outlet was directly at the end of the mixing channel.

A Newtonian glycerol solution was injected into the two inlets of the T-junction mixer. The fluid at one inlet contained 10 μg/mL of Rhodamine B, while the other did not, so the mixing degree could be determined by quantifying the Rhodamine B concentration. With the limit of one programmable pump (PHD ULTRA^{TM} 4400), we fixed the flow rate at 500 μL/h on one inlet, and modulated the flow rate on the other side under three different conditions: (i) Constant flow rate of 500 μL/h; (ii) alternating flow rate between 0 and 1000 μL/h at a frequency f = 0.5 Hz and duty cycle of 50%; (iii) alternating flow rate between 0 and 1000 μL/h at a frequency f = 0.1 Hz and duty cycle of 50%. The recorded flow pattern is shown in Figure 13b. The color map represents the Rhodamine B concentration, which is normalized from 0 to 1: Yellow denotes a concentration of 1 and blue, a concentration of 0. For case (i), the flow rates at both inlets were the same constant value and the mixing region was narrow, indicating a small degree of mixing. For case (ii), the mixing region was increased when the flow rate on one side alternated at f = 0.5 Hz. The mixing region was further increased when the frequency decreased to 0.1 Hz in case (iii). According to the normalized concentrations of Rhodamine B, the degree of mixing at different flow distances along the channel is calculated using Equation (20) and plotted in Figure 13c. The origin indicates the point at which the fluid enters the mixing channel. The degree of mixing gradually increases with the flow distance, and stabilizes at 0.20 for case (i), 0.25 for case (ii), and 0.37 for case (iii). This experimentally demonstrates the enhancement in mixing when the flow is modulated on one side compared to having a constant driving flow at both sides, which agrees well with the simulation results. This also confirms that mixing is increased as the alternating frequency decreases.

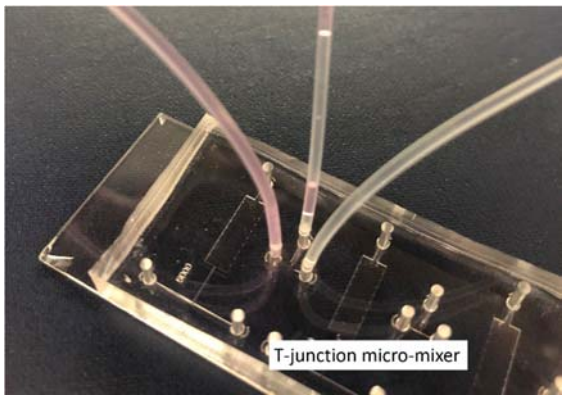

(**a**)

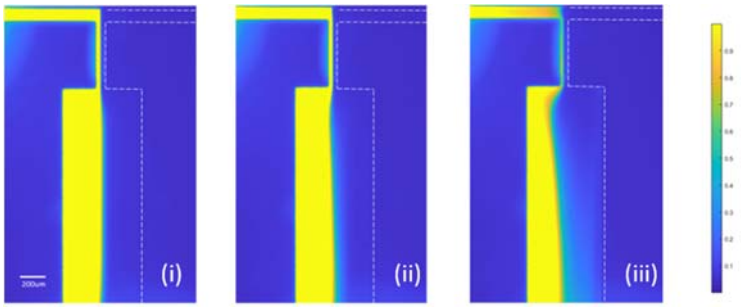

(**b**)

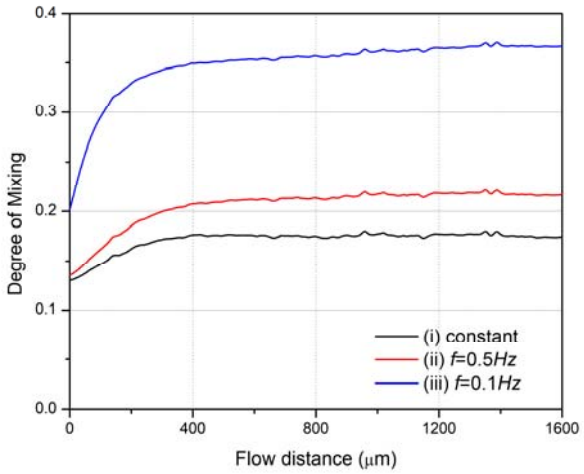

(**c**)

Figure 13. (**a**) The fabricated microfluidic chip for the T-mixer; (**b**) Recorded flow pattern of the glycerol solution with/without Rhodamine B on left/right side and the flow rate for right side (**i**) remains constant at 500 μL/h; (**ii**) alternates with frequency f = 0.5 Hz; (**iii**) alternates with frequency f = 0.1 Hz. (**c**) The measured degree of mixing for case (**i**–**iii**).

5. Conclusions

In conclusion: A T-junction micromixer was modeled, and mixing efficiencies were numerically compared for both a Newtonian fluid and a viscoelastic fluid as a function of driving pressure amplitude and modulation frequency. The degree of mixing is higher in a viscoelastic fluid than in a Newtonian fluid due to elastic stress in the viscoelastic fluid. Different modulations of the driving pressures at each inlet of the micromixer were explored. Under constant driving pressures, the degree of mixing was relatively low, 0.15 for the Newtonian fluid case and 0.25 for the viscoelastic fluid case.

When the driving pressures were modulated with a sinusoidal factor at one inlet while being held constant at the other, the degree of mixing increased to 0.62 and 0.67 for the Newtonian fluid and the viscoelastic fluid, respectively. When the driving pressures at both inlets of the micromixer were modulated with a sinusoidal factor, the mixing efficiency could be increased significantly by controlling the phase difference between the modulated pressures. The degree of mixing reached a maximum value of 0.82 using a viscoelastic fluid with a phase difference of π. Mixing enhancement arising from a low-frequency, single-inlet alternating modulation of the flow rate was experimentally demonstrated for a Newtonian glycerol solution. The method of modulating the driving pressure to enhance mixing may have potential applications in chemical engineering and in flow through porous media.

Author Contributions: M.Z. raised the original idea, wrote part of code for simulation software, analyzed the data, carried on the experiment, and wrote the paper. Y.C. simulated the data. W.C. revised the paper and coordinated this work. Z.W. did the experiment. Y.L. simulated the data. F.L. supervised on the simulation and the code for simulation software. W.Z. discussed the original idea, analyzed the simulation and experimental data, composed, and revised the paper.

Funding: This work is supported by this project is supported by the China Scholarship Council (No. 201606120130).

Conflicts of Interest: The authors declare no conflicts of interest.

References

1. Stroock, A.D.; Dertinger, S.K.W.; Ajdari, A.; Mezić, I.; Stone, H.A.; Whitesides, G.M. Chaotic mixer for microchannels. *Science* **2002**, *295*, 647–651. [CrossRef] [PubMed]
2. Lee, C.Y.; Fu, L.M. Recent advances and applications of micromixers. *Sens. Actuators B Chem.* **2018**, *259*, 677–702. [CrossRef]
3. Roberge, D.M.; Ducry, L.; Bieler, N.; Cretton, P.; Zimmermann, B. Microreactor technology: A revolution for the fine chemical and pharmaceutical industries? *Chem. Eng. Technol.* **2005**, *28*, 318–323. [CrossRef]
4. Ehrfeld, W.; Hessel, V.; Löwe, H. *Microreactors—New Technology for Modern Chemistry*; Wiley-VCH: Weinheim, Germany, 2000; p. 288. ISBN 3-527-29590-9.
5. Kefala, I.N.; Papadopoulos, V.E.; Karpou, G.; Kokkoris, G.; Papadakis, G.; Tserepi, A. A labyrinth split and merge micromixer for bioanalytical applications. *Microfluid. Nanofluid.* **2015**, *19*, 1047–1059. [CrossRef]
6. Lang, Q.; Ren, Y.; Hobson, D.; Tao, Y.; Hou, L.; Jia, Y.; Hu, Q.; Liu, J.; Zhao, X.; Jiang, H. In-plane microvortices micromixer-based AC electrothermal for testing drug induced death of tumor cells. *Biomicrofluidics* **2016**, *10*, 64102. [CrossRef] [PubMed]
7. Hessel, V.; Löwe, H.; Schönfeld, F. Micromixers—A review on passive and active mixing principles. *Chem. Eng. Sci.* **2005**, *60*, 2479–2501. [CrossRef]
8. Abed, W.M.; Whalley, R.D.; Dennis, D.J.C.; Poole, R.J. Experimental investigation of the impact of elastic turbulence on heat transfer in a serpentine channel. *J. Non-Newtonian Fluid Mech.* **2016**, *231*, 68–78. [CrossRef]
9. Ye, Y.; Chiogna, G.; Cirpka, O.A.; Grathwohl, P.; Rolle, M. Experimental investigation of transverse mixing in porous media under helical flow conditions. *Phys. Rev. E* **2016**, *94*, 13113. [CrossRef] [PubMed]
10. Ouyang, Y.; Xiang, Y.; Zou, H.; Chu, G.; Chen, J. Flow characteristics and micromixing modeling in a microporous tube-in-tube microchannel reactor by CFD. *Chem. Eng. J.* **2017**, *321*, 533–545. [CrossRef]
11. Li, J.S.; Li, Q.; Cai, W.H.; Li, F.C.; Chen, C.Y. Mixing Efficiency via Alternating Injection in a Heterogeneous Porous Medium. *J. Mech.* **2018**, *34*, 167–176. [CrossRef]
12. Cai, J.; Wei, W.; Hu, X.; Liu, R.; Wang, J. Fractal characterization of dynamic fracture network extension in porous media. *Fractals* **2017**, *25*. [CrossRef]
13. Elvira, K.S.; Solvas, X.C.; Wootton, R.C.R.; Demello, A.J. The past, present and potential for microfluidic reactor technology in chemical synthesis. *Nat. Chem.* **2013**, *5*, 905–915. [CrossRef] [PubMed]
14. Floquet, C.F.A.; Sieben, V.J.; MacKay, B.A.; Mostowfi, F. Determination of boron concentration in oilfield water with a microfluidic ion exchange resin instrument. *Talanta* **2016**, *154*, 304–311. [CrossRef] [PubMed]
15. Liu, R.; Jiang, Y.; Li, B.; Wang, X. A fractal model for characterizing fluid flow in fractured rock masses based on randomly distributed rock fracture networks. *Comput. Geotech.* **2015**, *65*, 45–55. [CrossRef]
16. Knight, J.B.; Vishwanath, A.; Brody, J.P.; Austin, R.H. Hydrodynamic focusing on a silicon chip: Mixing nanoliters in microseconds. *Phys. Rev. Lett.* **1998**, *80*, 3863–3866. [CrossRef]

17. Squires, T.M.; Quake, S.R. Microfluidics: Fluid physics at the nanoliter scale. *Rev. Mod. Phys.* **2005**, *77*, 977–1026. [CrossRef]
18. Xia, H.M.; Wang, Z.P.; Koh, Y.X.; May, K.T. A microfluidic mixer with self-excited 'turbulent' fluid motion for wide viscosity ratio applications. *Lab Chip* **2010**, *10*, 1712–1716. [CrossRef] [PubMed]
19. Lemenand, T.; Della Valle, D.; Habchi, C.; Peerhossaini, H. Micro-mixing measurement by chemical probe in homogeneous and isotropic turbulence. *Chem. Eng. J.* **2017**, *314*, 453–465. [CrossRef]
20. Wu, J.W.; Xia, H.M.; Zhang, Y.Y.; Zhu, P. Microfluidic mixing through oscillatory transverse perturbations. *Mod. Phys. Lett. B* **2018**, *32*. [CrossRef]
21. Stone, H.A.; Stroock, A.D.; Ajdari, A. Engineering flows in small devices: Microfluidics toward a lab-on-a-chip. *Annu. Rev. Fluid Mech.* **2004**, *36*, 381–411. [CrossRef]
22. Schönfeld, F.; Hessel, V.; Hofmann, C. An optimised split-and-recombine micro-mixer with uniform 'chaotic' mixing. *Lab Chip* **2004**, *4*, 65–69. [CrossRef] [PubMed]
23. Sivashankar, S.; Agambayev, S.; Mashraei, Y.; Li, E.Q.; Thoroddsen, S.T.; Salama, K.N. A "twisted" microfluidic mixer suitable for a wide range of flow rate applications. *Biomicrofluidics* **2016**, *10*. [CrossRef] [PubMed]
24. Lee, N.Y.; Yamada, M.; Seki, M. Development of a passive micromixer based on repeated fluid twisting and flattening, and its application to DNA purification. *Anal. Bioanal. Chem.* **2005**, *383*, 776–782. [CrossRef] [PubMed]
25. Jafari, O.; Rahimi, M.; Kakavandi, F.H. Liquid-liquid extraction in twisted micromixers. *Chem. Eng. Process.* **2016**, *101*, 33–40. [CrossRef]
26. Lin, M.X.; Hyun, K.A.; Moon, H.S.; Sim, T.S.; Lee, J.G.; Park, J.C.; Lee, S.S.; Jung, H.I. Continuous labeling of circulating tumor cells with microbeads using a vortex micromixer for highly selective isolation. *Biosens. Bioelectron.* **2013**, *40*, 63–67. [CrossRef] [PubMed]
27. Bensaid, S.; Deorsola, F.A.; Marchisio, D.L.; Russo, N.; Fino, D. Flow field simulation and mixing efficiency assessment of the multi-inlet vortex mixer for molybdenum sulfide nanoparticle precipitation. *Chem. Eng. J.* **2014**, *238*, 66–77. [CrossRef]
28. Niu, X.; Lee, Y.K. Efficient spatial-temporal chaotic mixing in microchannels. *J. Micromech. Microeng.* **2003**, *13*, 454–462. [CrossRef]
29. Burghelea, T.; Segre, E.; Bar-Joseph, I.; Groisman, A.; Steinberg, V. Chaotic flow and efficient mixing in a microchannel with a polymer solution. *Phys. Rev. E Stat. Nonlinear Soft Matter Phys.* **2004**, *69*. [CrossRef] [PubMed]
30. Simonnet, C.; Groisman, A. Chaotic mixing in a steady flow in a microchannel. *Phys. Rev. Lett.* **2005**, *94*. [CrossRef] [PubMed]
31. Cai, G.; Xue, L.; Zhang, H.; Lin, J. A review on micromixers. *Micromachines* **2017**, *8*, 274. [CrossRef]
32. Lee, C.Y.; Wang, W.T.; Liu, C.C.; Fu, L.M. Passive mixers in microfluidic systems: A review. *Chem. Eng. J.* **2016**, *288*, 146–160. [CrossRef]
33. Gan, H.Y.; Lam, Y.C.; Nguyen, N.T. Polymer-based device for efficient mixing of viscoelastic fluids. *Appl. Phys. Lett.* **2006**, *88*. [CrossRef]
34. Xu, K.; Liang, T.; Zhu, P.; Qi, P.; Lu, J.; Huh, C.; Balhoff, M. A 2.5-D glass micromodel for investigation of multi-phase flow in porous media. *Lab Chip* **2017**, *17*, 640–646. [CrossRef] [PubMed]
35. Needham, R.B.; Doe, P.H. Polymer Flooding Review. *J. Pet. Technol.* **1987**, *39*, 1503–1507. [CrossRef]
36. Xu, K.; Zhu, P.; Tatiana, C.; Huh, C.; Balhoff, M. A microfluidic investigation of the synergistic effect of nanoparticles and surfactants in macro-emulsion based EOR. In Proceedings of the SPE—DOE Improved Oil Recovery Symposium Proceedings, Tulsa, OK, USA, 11–13 April 2016.
37. Xu, K.; Zhu, P.; Colon, T.; Huh, C.; Balhoff, M. A microfluidic investigation of the synergistic effect of nanoparticles and surfactants in macro-emulsion-based enhanced oil recovery. *SPE J.* **2017**, *22*, 459–469. [CrossRef]
38. Olajire, A.A. Review of ASP EOR (alkaline surfactant polymer enhanced oil recovery) technology in the petroleum industry: Prospects and challenges. *Energy* **2014**, *77*, 963–982. [CrossRef]
39. Jha, B.; Cueto-Felgueroso, L.; Juanes, R. Fluid mixing from viscous fingering. *Phys. Rev. Lett.* **2011**, *106*. [CrossRef] [PubMed]
40. Jha, B.; Cueto-Felgueroso, L.; Juanes, R. Synergetic fluid mixing from viscous fingering and alternating injection. *Phys. Rev. Lett.* **2013**, *111*. [CrossRef] [PubMed]

41. James, D.F.; McLaren, D.R. The laminar flow of dilute polymer solutions through porous media. *J. Fluid Mech.* **1975**, *70*, 733–752. [CrossRef]
42. Peters, E.C.; Petro, M.; Svec, F.; Fréchet, J.M.J. Molded Rigid Polymer Monoliths as Separation Media for Capillary Electrochromatography. 1. Fine Control of Porous Properties and Surface Chemistry. *Anal. Chem.* **1998**, *70*, 2288–2295. [CrossRef] [PubMed]
43. Rodriguez, S.; Romero, C.; Sargenti, M.L.; Müller, A.J.; Sáez, A.E.; Odell, J.A. Flow of polymer solutions through porous media. *J. Non-Newtonian Fluid Mech.* **1993**, *49*, 63–85. [CrossRef]
44. Stavland, A.; Jonsbråten, H.C.; Lohne, A.; Moen, A.; Giske, N.H. Polymer flooding—Flow properties in porous media versus rheological parameters. In Proceedings of the 72nd European Association of Geoscientists and Engineers Conference and Exhibition 2010: A New Spring for Geoscience, Barcelona, Spain, 14–17 June 2010; pp. 3292–3306.
45. Liu, R.; Li, B.; Jiang, Y. Critical hydraulic gradient for nonlinear flow through rock fracture networks: The roles of aperture, surface roughness, and number of intersections. *Adv. Water Resour.* **2016**, *88*, 53–65. [CrossRef]
46. Liu, R.; Li, B.; Jiang, Y. A fractal model based on a new governing equation of fluid flow in fractures for characterizing hydraulic properties of rock fracture networks. *Comput. Geotech.* **2016**, *75*, 57–68. [CrossRef]
47. Li, Z.; Kim, S.J. Pulsatile micromixing using water-head-driven microfluidic oscillators. *Chem. Eng. J.* **2017**, *313*, 1364–1369. [CrossRef]
48. Glasgow, I.; Aubry, N. Enhancement of microfluidic mixing using time pulsing. *Lab Chip* **2003**, *3*, 114–120. [CrossRef] [PubMed]
49. Krupa, K.; Nunes, M.I.; Santos, R.J.; Bourne, J.R. Characterization of micromixing in T-jet mixers. *Chem. Eng. Sci.* **2014**, *111*, 48–55. [CrossRef]
50. Gao, Z.; Han, J.; Bao, Y.; Li, Z. Micromixing efficiency in a T-shaped confined impinging jet reactor. *Chin. J. Chem. Eng.* **2015**, *23*, 350–355. [CrossRef]
51. Liu, Z.; Guo, L.; Huang, T.; Wen, L.; Chen, J. Experimental and CFD studies on the intensified micromixing performance of micro-impinging stream reactors built from commercial T-junctions. *Chem. Eng. Sci.* **2014**, *119*, 124–133. [CrossRef]
52. Oualha, K.; Ben Amar, M.; Michau, A.; Kanaev, A. Observation of cavitation in exocentric T-mixer. *Chem. Eng. J.* **2017**, *321*, 146–150. [CrossRef]
53. Li, B.; Liu, R.; Jiang, Y. Influences of hydraulic gradient, surface roughness, intersecting angle, and scale effect on nonlinear flow behavior at single fracture intersections. *J. Hydrol.* **2016**, *538*, 440–453. [CrossRef]
54. Giesekus, H. A simple constitutive equation for polymer fluids based on the concept of deformation-dependent tensorial mobility. *J. Non-Newtonian Fluid Mech.* **1982**, *11*, 69–109. [CrossRef]

© 2018 by the authors. Licensee MDPI, Basel, Switzerland. This article is an open access article distributed under the terms and conditions of the Creative Commons Attribution (CC BY) license (http://creativecommons.org/licenses/by/4.0/).